CrossMark

Outlier Detection in the DESI Bright Galaxy Survey

Yan Liang[1] ✦, Peter Melchior[1,2] ✦, ChangHoon Hahn[1] ✦, Jeff Shen[1] ✦, Andy Goulding[1] ✦, and Charlotte Ward[1] ✦
[1] Department of Astrophysical Sciences, Princeton University, Princeton, NJ 08544, USA; yanliang@princeton.edu
[2] Center for Statistics & Machine Learning, Princeton University, Princeton, NJ 08544, USA

Abstract

We present an unsupervised search for outliers in the Bright Galaxy Survey (BGS) data set from the DESI Early Data Release. This analysis utilizes an autoencoder to compress galaxy spectra into a compact, redshift-invariant latent space, and a normalizing flow to identify low-probability objects. The most prominent outliers show distinctive spectral features, such as irregular or double-peaked emission lines or originate from galaxy mergers, blended sources, and rare quasar types, including one previously unknown broad absorption line system. A significant portion of the BGS outliers are stars spectroscopically misclassified as galaxies. By building our own star model trained on spectra from the DESI Milky Way Survey, we have determined that the misclassification likely stems from the principle component analysis of stars in the DESI pipeline. To aid follow-up studies, we make the full probability catalog of all BGS objects and our pretrained models publicly available.

1. Introduction

Large spectroscopic surveys, such as the Sloan Digital Sky Survey (SDSS; York et al. 2000), have gathered spectroscopic data for millions of astronomical objects. The next generation of surveys, such as the Dark Energy Spectroscopic Instrument (DESI; DESI Collaboration et al. 2016), produce even larger data sets. While the majority of cataloged objects can be classified using known spectral types, there also exist "unknown unknowns"—rare phenomena or object types that deviate from established physical models. In such cases, unsupervised machine-learning methods can identify features in the data without relying on predefined labels or predetermined templates. Such methods are particularly valuable for detecting outliers, which are, by definition, rare and often unexpected.

In this work, we search for outliers in the Early Data Release (EDR; DESI Collaboration et al. 2023a) of the DESI Bright Galaxy Survey (BGS; Hahn et al. 2023), which we briefly describe in Section 2. We employ the spectrum autoencoder (AE) architecture SPENDER introduced by Melchior et al. (2023). This technique compresses galaxy spectra into a compact, redshift-invariant latent space, representing the "type" of galaxies, and makes full use of the observed spectra across all redshifts. Following the approach of Liang et al. (2023), we interpret the sample density in the AE latent space as a probability distribution and identify outliers as low-probability objects using a normalizing flow (NF) model. We describe this approach in Section 3.

Our previous application of this method to SDSS galaxy spectra uncovered a range of astrophysical and instrumental outliers, including blends of multiple galaxies and/or stars, extremely reddened galaxies, as well as stars that had been misclassified as galaxies (Liang et al. 2023). With the new

DESI data set, we again expect outliers to correspond to galaxies in unusual physical states. We also expect them to reveal failures or artifacts of the data processing pipelines and therefore serve as an alternative mechanism for quality control, sensitive to problems that were not even known to be problems.

In Section 4, we present and discuss the nature of remarkable outliers in the BGS galaxy sample, including merging galaxies and rare quasars. Our visual inspection also reveals a substantial fraction to be misclassified stars. In Section 5, we extend our generative modeling approach to stellar spectra from the DESI Milky Way Survey (MWS; Cooper et al. 2023) and identify the likely reason why some BGS galaxies were misclassified. We conclude in Section 6 with a discussion of the limitations and potential extensions of this study.

2. Data

We use data from the DESI EDR, which includes spectra observed during the Survey Validation (SV) campaign that was conducted before the start of the main survey to evaluate DESI's scientific program (DESI Collaboration et al. 2023b). SV was divided into two main phases: an initial "Target Selection Validation" phase to finalize the target selection and a pilot survey of the full DESI program that covered $\sim$140 deg^2, the One-Percent Survey.

In this work, we focus on targets from the BGS and the MWS. The initial target lists are defined on the basis of the imaging data from the Legacy Surveys (LS; Dey et al. 2019). An object is considered a BGS target if it is either not in the Gaia Data Release 2 catalog (Gaia Collaboration et al. 2018) or if it is in Gaia and has $(G_{Gaia} - r_{raw}) > 0.6$, where G_{Gaia} is the G-band magnitude from Gaia and r_{raw} is the LS r-band magnitude without galactic extinction correction. Afterward, a fiber-magnitude cut is imposed to remove imaging artifacts or other spurious objects. Quality cuts then remove any object without photometric observations in all three LS optical bands and with colors outside $-1 < (g - r) < 4$ and $-1 < (r - z) < 4$. Very bright objects with $r > 12$ and $r_{fibertot} < 15$ are also
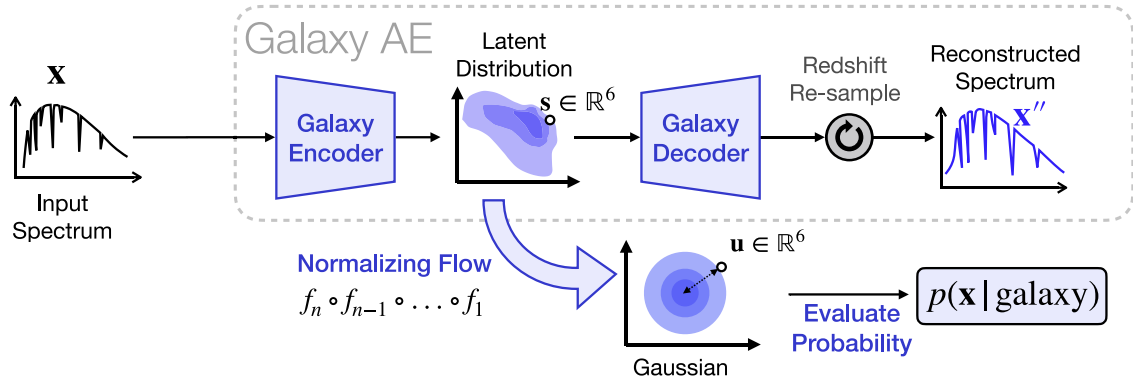
Figure 1. Our approach combines an AE for spectrum reconstruction and an NF for probability estimation. The AE compresses an observed galaxy spectrum into a low-dimensional latent representation of the restframe spectrum, and the NF transforms the latent distribution of the entire BGS galaxy sample into a Gaussian base distribution for efficient probability computation and sampling.

removed from the sample. For further details on the BGS target selection, see Hahn et al. (2023).

MWS targets consist of objects that are in both LS and Gaia Early Data Release 3 (Gaia Collaboration et al. 2021). They are restricted to objects that are classified as point sources based on their morphology and within the magnitude limits $16 < r < 19.2$ and $r_{\mathrm{raw}} < 20$. There is an additional cut on Gaia astrometric excess noise (Gaia AEN < 3) as well as quality cuts on the LS g- and r-band photometry. No quality cuts on z-band photometry are imposed. For further details on the MWS target selection, see Cooper et al. (2023).

All spectra in the EDR are reduced using the "fuji" version of the DESI spectroscopic data reduction pipeline (Guy et al. 2023). First, spectra are extracted from the spectrograph charge-coupled devices (CCDs) using the *spectroperfectionism* algorithm of Bolton & Schlegel (2010). Then, fiber-to-fiber variations are corrected by flat-fielding, and a sky model, empirically derived from sky fibers, is subtracted from each spectrum. Afterwards, the fluxes in the spectra are calibrated using stellar model fits to standard stars. The calibrated spectra are coadded across exposures to produce the final processed spectra. Among the different coadds in the EDR, we use the ones produced by combining all available spectra for a given target.

For each spectrum, the DESI EDR provides redshift measurements from the *Redrock*[3] redshift fitting algorithm. For a given spectrum, *Redrock* derives redshift by minimizing the χ^2 between the observed spectrum and a model spectrum constructed from a linear combination of principal component analysis (PCA) basis spectral templates in three template classes ("stellar," "galaxy," and "quasar"). The redshift and template class that produces the lowest χ^2 is used as the best-fit redshift and spectral classification. *Redrock* also provides an estimate of redshift uncertainties, ZERR, and a redshift confidence measurement, $\Delta\chi^2$, which corresponds to the difference between the χ^2 values of the best-fit model and the next-best-fit model.

For BGS, we only use spectra observed with functioning fiber positioners and with reliable redshift measurements as defined in Hahn et al. (2023). We only keep spectra classified as galaxy spectra by *Redrock* (i.e., SPECTYPE == ``GALAXY'') with redshifts $z \in [0, 0.8]$ (cutting off a very minor high-redshift tail) and having no

Redrock warning flags ZWARN. From MWS, we select spectra with ZWARN == 0 and SPECTYPE == ``STAR.''

With those cuts, we compile approximately 250,000 BGS and 210,000 MWS spectra. The observed wavelength range is $\lambda_{\mathrm{obs}} = 3600...9824$ Å. We split the samples into training, validation, and testing sets, each accounting for 70%, 15%, and 15% of the entire samples, respectively. We adopt the inverse-variance weights and masks from the DESI EDR as data weights (w). We apply an additional mask to the top $\sim$100 telluric lines, assigning zero weights to all bins within 5 Å of the line centers, which amounts to approximately 25% of the data vectors. The spectra are then normalized by the median flux over the rest-frame wavelengths $\lambda_{\mathrm{rest}} = 5300...5850$ Å, a region that is relatively quiescent and accessible at all redshifts, thereby avoiding redshift-dependent encoding.

3. Methods

Our general approach follows Liang et al. (2023) and is summarized in Figure 1. In short, we train the spectrum AE architecture SPENDER (Melchior et al. 2023) on the observed BGS spectra. That means we encode a spectrum $x \in \mathbb{R}^M$ into a small number of latent variables $s \in \mathbb{R}^S$. For this work, we set $S = 6$. From these latents, the decoder produces a restframe model x', which is redshifted and resampled to produce an observed-frame reconstruction x'' that matches the observation. In the first training phase, we adjust the network weights so as to minimize the fidelity loss, which quantifies the reconstruction quality over batches of N spectra:

$$L_{\mathrm{fid}} = \frac{1}{2NM} \sum_i^N w_i \odot (x_i - x_i''(x_i, z_i))^2, \qquad (1)$$

where x_i and x_i'' denote the input spectrum and its observed-frame reconstruction z_i is the known redshift of source i, w_i is the inverse variance weights from EDR with telluric masks, and $\odot$ is the element-wise multiplication. For Gaussian-distributed noise, this loss measures the mean log-likelihood of data given the AE model.[4]

In the second phase, we train with the fidelity loss and two extra losses that make the latent space distribution

---

[4] As described by Guy et al. (2023), the flux errors provided by the EDR are uncorrelated with wavelength and well-approximated by Gaussian distribution. While we recognize that real flux errors may show some deviations from perfect Gaussianity, our framework can adapt to alternative noise distributions by changing the likelihood model in the loss function.
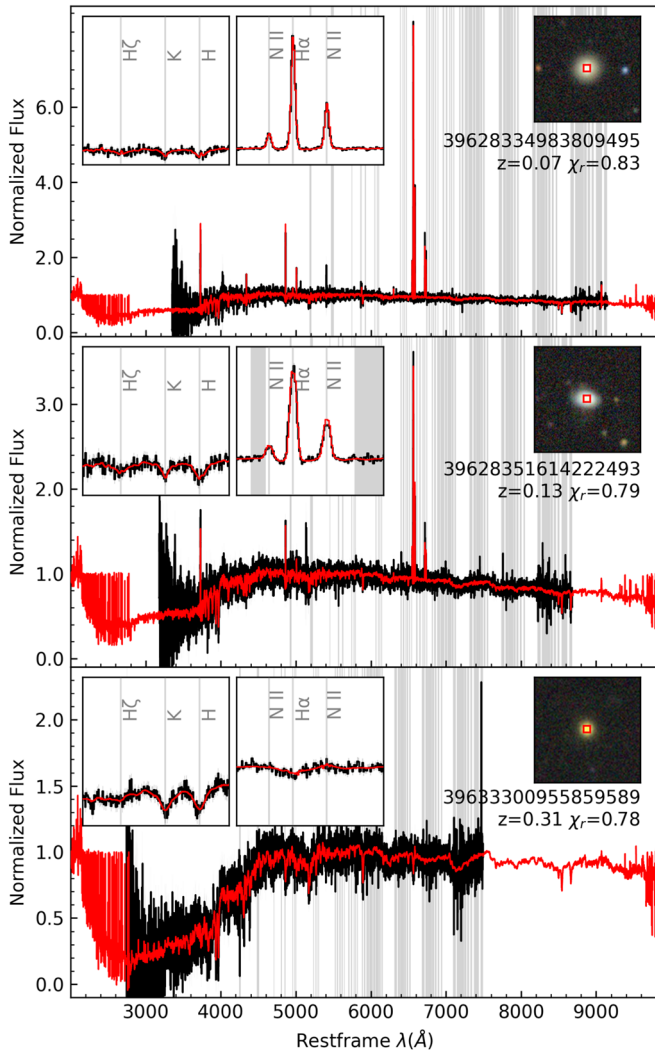
Figure 2. BGS galaxy spectra (black) and their reconstructed models (red) as determined by our spectrum AE. The main panels present the entire flux-normalized restframe spectrum, assuming the *Redrock* redshift, with regions masked during training shaded in gray. The upper left panels provide zoomed-in views of significant emission/absorption lines, while the upper right panels show the image of the source from the DESI Legacy Imaging Surveys with the fiber size indicated in red.

approximately redshift-invariant. This property yields a more physically meaningful latent distribution and has proven effective for finding outliers in SDSS spectra (Liang et al. 2023). The first extra loss term ensures that spectra that are close in data space are also close in latent space; the second one promotes proximity in latent space between the original spectrum and an augmented version, where we modified the redshift and added additional noise to the spectrum (see additional details about loss functions in Liang et al. 2023).

Upon convergence of our two-phase training, we achieved fidelity losses of 0.384, 0.391, and 0.386 on the training, validation, and test sets, respectively. The consistency across different data sets indicates that our model is generalizing well on unseen data points, with no evidence of significant overfitting. The achieved fidelity corresponds to a reduced chi-square (χ^2) value of 0.77. Figure 2 presents the reconstructed restframe models for three representative galaxy spectra in BGS. As intended, the model also exhibits redshift invariance. In the latent space of the trained AE model, original

spectra and their artificially redshifted augmentation spectra are, on average, 21 times closer to each other than the average pairwise distance between different objects. This indicates that our model successfully captures the intrinsic characteristics of galaxies, regardless of their redshift.

In Figure 2, the reconstructed spectra exhibit larger spreads at both the shortest and longest wavelengths. This behavior results from the lack of extremely high and low redshift samples in our data set. In these regions, the under-constrained model produces many "spikes," which gravitate toward 1—the default value from the decoder's initialization. While this suggests that model predictions at the edges of the wavelength range should be used with caution, the central rest-frame range, where the bulk of the galaxy spectra lie, is reliably captured by our model.

As the last step, we train a specific type of NF (Tabak & Vanden-Eijnden 2010; Tabak & Turner 2013) model known as a Masked Autoregressive Flow (MAF; Papamakarios et al. 2017) to describe the density of galaxies in the AE latent space. The combination of an AE and an NF is synergistic. The NF provides a flexible density estimator for the complex latent distributions AEs tend to form, while the AE serves as a nonlinear compression scheme to provide a lower-dimensional space for the NF to operate in. Because of our extended training procedure, the latents are approximately invariant under changes of redshift, rendering them much more informative conditioning variables to describe intrinsic galaxy properties than the observed spectrum data vector. With the AE–NF combination, we can evaluate the probability $p_{\text{galaxy}} = p(\boldsymbol{x}|\text{BGS})$ of any spectrum $\boldsymbol{x}$ to be drawn from the BGS sample. Spectra with low p_{galaxy} can thus be interpreted as outliers in the galaxy sample.

4. BGS Outliers

We defined an outlier score as $-\log p_{\text{galaxy}}$ and carried out a visual inspection of the top 200 outliers. During our inspection, we employed a nonexclusive labeling approach, acknowledging that a single object can manifest multiple outlying behaviors and be tagged with several labels. For a complete list of these outliers, including their DESI ID, R.A., decl., outlier score, and visual labels, we direct the reader to Table 1 in the Appendix. A selection of these outliers is shown in Figure 3.

We identified velocity structures in 61 objects (30.5%). A significant fraction of the outliers are stars: 32 misclassified individual stars, 3 star pairs, and 5 star–galaxy blends. We also found 17 quasars (8.5%), including 2 unusual broad absorption line (BAL) quasars. Calibration or sky-subtraction anomalies were detected in 37 cases (18.5%). Wolf–Rayet signatures and [N I]λ5200 emissions were present in 42 (21%) and 27 (13.5%) of the objects, respectively. Narrow emission lines are observed in 17 cases (8.5%), 12 of which are extragalactic H II regions. Extreme starbursts, characterized by a distinctive blue continuum shape dominated by early-type stars, are detected in 26 (13%) objects. A smaller fraction of galaxies exhibited strong Hδ absorption (1%), extremely reddened continua (2%), or galaxy superposition features (1.5%). We found eight instances (4%) where the continuum seemed unusual for unclear reasons. Lastly, 1.5% of the outliers remained unidentified. The total exceeds 100% due to the multiple labels an object can receive.

Table 1
The Positions and Visual Classification Labels of the Top 200 DESI BGS Outliers Ranked by Their Negative Log Probabilities $-\log p_{\text{galaxy}}$

Rank	DESI ID	R.A.	Decl.	$-\log p$	Label	Reference
1	39633393184408234	191.21639606	60.52195792	56.41	Star Blend	
2	39633127651410738	241.19113199	42.84971658	32.62	AGN, Velocity Structure, WR	
3	39633404945237391	190.05019309	61.60006834	32.28	Starburst, H II Region, Narrow Line	
4	39633149726034475	247.03667189	44.10677520	32.02	Calibration, Velocity Structure	
5	39633158374688229	245.13714079	44.38041175	30.96	Quasar	
6	39633149658924999	241.46246538	44.09456197	27.95	AGN, Velocity Structure, WR	
7	39633275194442655	213.91675898	51.79208545	23.69	Star, Calibration	
8	39627823501017204	151.00310538	1.56949463	22.24	Star Blend	
9	39627794417717430	217.69175718	0.24769831	21.66	AGN, Velocity Structure, NI5200	
10	39633154058748211	245.82628960	44.12591853	21.16	Calibration	
11	39627896888755461	208.38156704	4.46808882	20.77	Velocity Structure	Kim02[a]
12	39633145246517940	237.82821998	43.77637695	20.76	Star, Unusual Continuum	
13	39627806434395296	213.80539212	0.67255028	20.69	AGN, Velocity Structure, WR	
14	39632956888715615	253.77379555	33.74953453	20.43	Star	
15	39627782380067362	220.23837742	−0.16430134	19.79	Quasar	
16	39633123218032296	242.74607607	42.62281998	19.63	Star	
17	39633145233934226	236.71242077	43.78182730	19.34	Starburst, WR	
18	39627793763402920	178.55114654	0.13666287	19.29	Starburst, WR	
19	39633416949335633	267.50840284	62.38214111	19.19	Starburst, WR, NI5200	
20	39627788356946460	216.36899370	−0.02289930	18.96	Galaxy Blend, Velocity Structure	DP07[b]
21	39632991718212824	252.02154620	35.41429522	18.93	Star, Unusual Continuum	
22	39633278931569179	213.87773842	52.07764608	18.90	Quasar	
23	39632981354087949	216.97411952	34.88008970	18.86	Quasar	
24	39633456321269541	272.43910763	66.36718521	18.74	Star–Galaxy Blend	
25	39627746015447627	212.63646004	−1.70980686	18.55	Velocity Structure, WR	
26	39633123197062964	241.21466636	42.56176786	18.52	Narrow Line	
27	39627818572714391	217.45314060	1.13999861	18.40	Unusual Continuum	
28	39627800432346105	216.03759188	0.39687948	18.26	Unknown	
29	39633290071641162	217.36368305	52.64709108	18.05	BAL Quasar	Liu15[c]
30	39633404945237394	190.05053314	61.59848457	18.00	Starburst, H II Region, Narrow Line	
31	39633154041974595	244.70627841	44.14650102	17.33	Calibration	
32	39633123171896770	239.14359548	42.57721712	16.99	Star–Galaxy Blend	
33	39632936152072650	217.98489545	32.86046815	16.72	AGN, Velocity Structure, WR	
34	39633325958106929	244.18292740	55.15161744	16.68	Star–Galaxy Blend	
35	39627817452833923	150.63910825	1.15066659	16.55	Calibration	
36	39633421919584704	191.01869183	63.08309401	16.43	Star, Calibration	
37	39627734065874069	220.29810317	−2.20977638	16.43	Starburst, Velocity Structure	Nordin20[d]
38	39633154037780536	244.39597331	44.15023335	16.15	Calibration	
39	39633465888476631	271.82308297	67.30025900	15.89	Star	
40	39633339602177656	244.42968225	56.28921387	15.86	Star	
41	39633140855081990	237.28833071	43.58263535	15.82	AGN, Velocity Structure, WR	
42	39633404945236638	189.97944301	61.61185836	15.75	Narrow line, H II Region	
43	39633402051166367	191.39696481	61.33389955	15.72	Velocity Structure, NI5200	
44	39633308396555667	241.31654041	53.90300579	15.53	AGN, Velocity Structure, WR	
45	39633404945237128	190.02788359	61.60073645	15.52	Starburst, H II Region, Narrow Line	
46	39633118776266593	245.22034212	42.15568048	15.49	Star	
47	39633123239003574	244.37623708	42.45819402	15.46	Star	
48	39627872935085865	218.38706314	3.60292414	15.43	WR, NI5200	
49	39633339585399522	242.59977716	56.30874655	15.38	Star	
50	39633114233831810	241.04065227	41.98934740	15.37	Star	
51	39627782338122510	217.72209497	−0.15486698	15.36	AGN, Velocity Structure, WR, NI5200	
52	39632956397979794	218.53966120	33.78019707	15.30	AGN, Velocity Structure, WR	
53	39633416341160166	189.19099207	62.53105078	15.24	Star, Calibration	
54	39633458753962651	272.28340341	66.38409905	15.18	Strong Hδ, Blue-skewed Emission	
55	39627770313048320	220.75926227	−0.73406376	15.16	AGN, Velocity Structure, WR	
56	39628454588580337	195.11869341	28.83631683	14.93	Star	
57	39633308396554942	241.25875691	53.94205561	14.91	Star	
58	39627788289840013	212.47311474	−0.08632021	14.77	Calibration	
59	39628362636858151	193.43361885	24.57301782	14.66	Starburst	
60	39633407830920247	190.40092966	61.67871863	14.63	AGN, Velocity Structure, WR, NI5200	KW20[e]
61	39633158282412508	237.37165164	44.38003234	14.62	Starburst, NI5200	
62	39632981370864866	218.16481755	35.03089174	14.51	Velocity Structure, NI5200	
63	39628427891835918	193.55098915	27.62475284	14.39	WR, High-ionization Region	Capetti22[f]
64	39627788302418655	213.03300186	0.05699578	14.39	AGN, Velocity Structure, WR	

Table 1
(Continued)

Rank	DESI ID	R.A.	Decl.	$-\log p$	Label	Reference
65	39633118805624111	247.39976984	42.25962869	14.33	Quasar	
66	39633318987170762	241.83017570	54.86026842	14.29	Narrow Line	
67	39633149713452510	246.09106992	44.11576396	14.27	Calibration	
68	39633123243197863	244.73971945	42.50974232	14.18	Star Blend	
69	39627776273159194	216.23395818	−0.37606986	14.13	Starburst, Velocity Structure	
70	39627746028029464	213.31377023	−1.70581552	14.03	AGN, Velocity Structure, WR	
71	39633297331980333	213.49720421	53.19452851	14.02	Strong Hδ, Velocity Structure	
72	39632961397589795	216.86655031	34.08542460	14.00	Star–Galaxy Blend	
73	39633408472647295	270.43592434	61.85989911	13.87	Unusual Continuum	
74	39627794430300571	218.46425449	0.27041670	13.82	Calibration	
75	39633149713449687	245.83135908	44.09902712	13.82	Calibration	
76	39633411316386675	268.77219598	61.93145582	13.81	Star	
77	39627781784471770	184.61129914	−0.13059894	13.77	AGN, Velocity Structure, WR, NI5200	
78	39627811891187010	179.19058826	1.01424993	13.74	Narrow Line	
79	39627763644106528	183.33361727	−1.07886881	13.63	Velocity Structure	
80	396333329372269015	240.87147942	55.49844166	13.62	Star, Unusual Continuum	
81	39627806405036766	212.11517350	0.80428030	13.58	Quasar	
82	39633149738615189	247.87659809	44.06179387	13.58	Calibration	
83	39627739971455294	212.37018340	−1.90638843	13.55	Dusty	
84	39628334988006041	194.10612279	23.34861120	13.54	Dusty, NI5200	BH12[g]
85	39628334988004771	194.03626748	23.27075384	13.52	Velocity Structure, WR	
86	39633427976161097	269.39238615	63.41707817	13.44	Unknown	
87	39633154041974645	244.71013731	44.16033849	13.43	Calibration	
88	39632976899738586	253.93567727	34.76404245	13.43	Dusty, Velocity Structure	
89	39633140972521107	246.74848571	43.59339370	13.41	Calibration	
90	39633123209645494	242.20719882	42.38255377	13.31	Negative Flux	
91	39627794400937953	216.58546120	0.34932122	13.30	Velocity Structure, WR, NI5200	
92	39628470426273307	194.11751938	29.41044222	13.28	Starburst, WR	
93	39633162686433333	245.41970374	44.82164212	13.27	Star–Galaxy Blend	
94	39633458712020311	266.17297332	66.50413193	13.23	Starburst	
95	39627758216676628	219.79775734	−1.23326355	13.22	Velocity Structure, NI5200	
96	39627757612696880	183.81423614	−1.16199449	13.21	AGN, Velocity Structure, WR	
97	39633149730227229	247.24230746	44.07986088	13.14	Calibration	
98	39633149726033986	246.99798460	44.09669949	13.14	Calibration	
99	39633136539142572	244.22902860	43.35838691	13.11	AGN, Velocity Structure, WR, NI5200	
100	39627806476342186	216.46446529	0.84513999	13.07	Quasar	
101	39632946797218283	253.59800161	33.30089600	13.02	Velocity Structure, NI5200	
102	39627853658067307	148.74381397	2.65691350	13.02	Calibration	
103	39633399098376582	188.75785940	60.88318264	12.92	Star	
104	39633329372269773	240.96373129	55.39628241	12.88	AGN, Velocity Structure, WR, NI5200	
105	39633421923780182	191.76082536	62.92033333	12.87	AGN, Velocity Structure, WR	
106	39633416345356485	190.04132117	62.56152098	12.85	AGN, Velocity Structure, WR	
107	39633127701745009	245.46062004	42.63918331	12.81	AGN, Velocity Structure, WR	
108	39627884863687260	210.43473602	3.96388773	12.81	Starburst, H II Region, Narrow Line	
109	39632941231378390	218.07871377	33.04850095	12.80	Starburst, H II Region, Narrow Line	
110	39627769679708271	183.00211259	−0.77090542	12.80	Galaxy Blend	
111	39627746002864250	211.85313793	−1.64602660	12.77	Reddened Quasar, Blue-skewing Emission	
112	39633413543562464	191.74306680	62.37470049	12.76	Quasar	
113	39633308400747093	241.46820727	54.11432578	12.73	Starburst, NI5200	
114	39633149709258216	245.72802838	44.08576066	12.71	Calibration	
115	39627939041510701	209.98345844	6.24173726	12.67	BAL Quasar	
116	39627764269056634	220.52253960	−0.88012705	12.65	Starburst	
117	39632946767856971	251.42905685	33.28504057	12.64	Velocity Structure, WR	
118	39627902953722577	211.06694675	4.83131139	12.63	AGN, Velocity Structure, WR	
119	39633422515179983	269.17518405	62.91246556	12.61	Star	
120	39627782380061799	220.04243681	−0.28926018	12.57	Narrow Line, H II Region, NI5200	
121	39633136585277790	247.77854993	43.33653911	12.49	Starburst, H II Region, Narrow Line	
122	39632991705631163	251.16732035	35.51944242	12.49	Star	
123	39633470514791272	269.15790270	67.67441180	12.48	Calibration	
124	39627878945523536	217.13300805	3.73687543	12.47	Star	
125	39627800390405432	213.67290697	0.44538149	12.46	Galaxy Blend, Velocity Structure	
126	39628346086131599	194.28510670	23.73651061	12.45	Quasar	
127	39633153928725824	235.14409365	44.19942477	12.45	Starburst, Velocity Structure	
128	39632981823848928	250.99980040	34.93168817	12.44	AGN, Velocity Structure, WR	

Table 1
(Continued)

Rank	DESI ID	R.A.	Decl.	$-\log p$	Label	Reference
129	39633301241072951	242.67059084	53.37794635	12.42	Star	
130	39633443771910388	267.95869388	65.05233119	12.34	Velocity Structure, NI5200	
131	39633149738616628	247.98493895	43.98783780	12.31	Calibration	
132	39633393184410015	191.45146352	60.54739112	12.31	NI5200	
133	39633154075526488	247.30529368	44.24523232	12.31	AGN, Velocity Structure, WR	
134	39628459860824965	193.67401048	28.94530107	12.27	Narrow Line, H II Region	
135	39633419134568709	189.59931486	62.87107553	12.26	AGN, Velocity Structure, WR	
136	396333332824178943	243.70462100	55.75349884	12.25	AGN, Velocity Structure, WR	
137	39633422506788684	267.76052868	62.97478250	12.25	Star	
138	39633410683045993	188.79793322	61.96384723	12.22	Star	
139	39628335013170846	195.66957628	23.36939498	12.19	AGN, Velocity Structure, WR	
140	39633154058750552	246.02518274	44.14271727	12.14	Calibration	
141	39633145355570265	246.77708709	43.64185269	12.12	Velocity Structure	
142	39633145322015404	244.02415566	43.70643864	12.12	Calibration	
143	39627800499456537	220.11511049	0.46762544	12.10	Calibration	
144	39628368143977513	193.91672392	24.74515096	12.07	WR	
145	39633158261444242	235.90345586	44.46636580	12.05	Narrow Line	
146	39633413505811189	186.49706642	62.18815795	12.05	Star	
147	39628390055023889	195.48083738	25.81863701	12.05	Velocity Structure	
148	39627841603636009	150.09559784	2.22013312	12.02	Starburst	
149	39627902957912300	211.09580292	4.76928931	11.98	Quasar	
150	39628362632661554	193.03110532	24.38839629	11.97	Starburst	
151	39627746069975548	215.98272141	−1.71377035	11.95	Velocity Structure	
152	39632971396812279	216.26744333	34.54023403	11.94	Velocity Structure	
153	39633339572816483	241.21909102	56.23202023	11.89	Star	
154	39633408468454516	270.12383932	61.64791291	11.86	Quasar	
155	39633118650436955	235.13246894	42.35214453	11.81	AGN, Velocity Structure, WR	
156	39633154050361018	245.23495147	44.13173757	11.79	Calibration	
157	39633408489427141	272.78746399	61.68179486	11.72	Star	
158	39633311978492123	244.81312218	54.23280039	11.69	Velocity Structure	
159	39633136417507647	234.30495422	43.29388884	11.68	Narrow Line, H II Region	
160	39627884855301487	210.03757637	4.08073882	11.67	Starburst, NI5200	
161	39627782245846352	212.13673149	−0.23354197	11.67	NI5200	
162	39627836704691291	218.23909763	2.05678596	11.67	Quasar	
163	39633315497511951	243.68620561	54.41039335	11.63	Calibration	
164	39628400926654536	195.02635486	26.28079769	11.62	Narrow Line	
165	39633405599549945	271.58349289	61.49632522	11.61	Quasar	
166	39627764151619120	213.65391532	−0.91641277	11.60	AGN, Velocity Structure, WR	
167	39633411320578585	269.00464064	61.96277487	11.60	Star	
168	39633446309463909	266.39553911	65.34438286	11.58	Star	
169	39633263865629351	215.52946228	50.96586133	11.54	Starburst	
170	39627800499457925	220.17512949	0.55597776	11.51	Calibration	
171	39633149713450070	245.87077389	44.10293008	11.50	Calibration	
172	39633162699014294	246.32535592	44.85487233	11.50	Calibration	
173	39633297365534734	216.80571009	53.16086873	11.49	Velocity Structure, NI5200	
174	39632956397978143	218.42867493	33.64768115	11.45	Quasar	
175	39633297340368987	214.33030076	53.13576164	11.39	AGN, Velocity Structure, WR	
176	39633411307996687	267.53410362	62.08505444	11.36	Velocity Structure	
177	39628465170812017	195.29140853	29.16919269	11.35	Velocity Structure, WR	
178	39627854849248939	219.67340028	2.68409817	11.34	Starburst	
179	39627776327685362	219.46894852	−0.39866647	11.34	Narrow Line, H II Region, NI5200	
180	39633304843977104	243.11838155	53.68355811	11.34	Star	
181	39633149738614936	247.85632193	44.04268988	11.31	Calibration	
182	39633136551724288	245.11255633	43.16990901	11.30	Star	
183	39633127626245269	239.18739916	42.77306283	11.29	Calibration	
184	39633275211219113	215.44865872	51.67300737	11.29	Starburst, Velocity Structure	
185	39627740042759428	216.64795386	−1.95534992	11.23	Velocity Structure	
186	39633149726032719	246.88093386	44.07519206	11.23	Calibration	
187	39633396145587770	189.36607795	60.74302125	11.22	Star, Calibration	
188	39633408472649705	270.67478642	61.63873022	11.22	Starburst	
189	39628351622611907	194.52695103	23.90235221	11.22	Starburst, H II Region, Narrow Line	
190	39633158332747293	241.79212470	44.43805378	11.21	Calibration	
191	39627781759307042	183.16638255	−0.21568462	11.17	AGN, Velocity Structure, WR, NI5200	
192	39627865754439330	149.87399876	3.18654127	11.11	NI5200	

<div align="center">

Table 1
(Continued)

</div>

Rank	DESI ID	R.A.	Decl.	$-\log p$	Label	Reference
193	39632996172563489	217.85999314	35.81165056	11.09	AGN, Dusty, Velocity Structure	
194	39627782350701872	218.31360160	−0.26680391	11.09	Unknown	
195	39627794438687394	218.85557115	0.33446441	11.07	NI5200	
196	39633416978694667	271.13334522	62.48835527	11.05	Unusual Continuum	
197	39627788382112558	217.87402328	−0.10771600	11.05	Calibration	
198	39627775727900051	183.71193052	−0.48924916	11.05	Calibration	
199	39627763572804616	179.14452002	−1.07581722	11.05	Unusual Continuum	
200	39627757587530223	182.27269517	−1.20514176	11.04	AGN, Velocity Structure, WR	

Notes.
[a] Kim et al. (2002).
[b] De Propris et al. (2007).
[c] Liu et al. (2015).
[d] Nordin et al. (2020).
[e] Kozieł-Wierzbowska et al. (2020).
[f] Capetti et al. (2022).
[g] Best & Heckman (2012).

(This table is available in machine-readable form.)

4.1. Velocity Structure

Velocity structures, loosely defined by irregularly shaped emission lines in their spectra, stand out as a dominant outlier type. A fraction of these outliers show double-peaked narrow emission lines (e.g., outlier 9,[5] shown in the second row of Figure 3), indicating that the spectra contain overlapping galaxies in cluster environments or galaxy mergers. Another example not shown in the figure, outlier 125, reveals two distinct sets of emission lines, and the DESI imaging data are consistent with a galaxy merger. Double-peaked narrow emission lines can arise due to complex kinematics in the narrow-line region surrounding a single AGN induced by outflows or disk rotation, or the presence of two separate narrow-line regions associated with two merging AGN at small relative velocities (Shen et al. 2011). Among the objects showing double-peaked emission lines, most galaxies have settled galaxy morphologies and no obvious mergers, making them candidates for close separation dual AGN in the late stages of the merger. The emission-line ratio diagnostics seem to offer some support for this hypothesis: of the 13 systems with double-peaked emission lines, 7 align with AGN classifications, which will be discussed in more detail below.

We further characterize these outliers using their emission-line ratios. The equivalent widths of prominent emission lines, such as [N II], [O III], [S II], Hα, and Hβ, were determined by fitting Gaussian profiles to the observed lines at fixed wavelengths and then integrating over these best-fit profiles. Following the classification scheme of Kewley et al. (2001), objects that lie above the empirical boundaries on the [N II]/Hα versus [O III]/Hβ and [S II]/Hα versus [O III]/Hβ diagrams were classified as "AGN" type. We found that 32[6] out of 61 objects align with AGN classifications in the Baldwin–Phillips–Terlevich (BPT) diagram.

A fraction of the sample is characterized by significantly broadened emission lines (FWHM >800 km s^{-1}). Such broadened emission lines can act as observational proxies of powerful AGN-driven outflows. For example, outlier 37 (Transient Name Server (TNS) AT2020dig) shows complex structures near the Hα and [O III] emissions involving multiple broad components that exceed 1000 km s^{-1}. This system was reported on the TNS (Nordin et al. 2020) due to the detection of AGN-like optical variability in time-domain imaging from the Zwicky Transient Facility (Bellm et al. 2019; Graham et al. 2019).

Lastly, some outliers demonstrate asymmetric emission lines —signatures of complex gas kinematics. For example, outlier 20 exhibits additional structure to the blue of its emission line centers. This is consistent with the DESI imaging data, which shows a close galaxy pair with evident tidal deformations. Furthermore, these observations align well with the system's prior classification as a galaxy merger by De Propris et al. (2007). Outlier 11 (SDSS J135331.57+042805.2, $z = 0.14$) stands out with asymmetric emission lines coupled with a reddened continuum. Its high star formation rate (SFR = 221.86 $M_\odot$yr^{-1}; Lai et al. 2020) positions it well above the star formation main sequence at low redshift (Lee et al. 2015; Renzini & Peng 2015). Such intense star formation is likely the primary driver behind its bright polycyclic aromatic hydrocarbon emission (Lai et al. 2020). Additionally, the reddened continuum and tidal features in the DESI imaging are consistent with its identification as an ultraluminous infrared galaxy undergoing a merger (Kim et al. 2002). In contrast, outlier 60 displays a combination of blue-skewing [O III] emission profile, Wolf–Rayet signature, and an extremely blue continuum in its optical spectrum. These spectral characteristics suggest ongoing starburst and AGN activity, which align with its recognition as a radio-loud AGN by Kozieł-Wierzbowska et al. (2020).

4.2. Quasar

In the top 200 BGS galaxy outliers, we visually identified 17 quasars. This group comprises two BAL quasars and one red/dust-obscured quasar. The *Redrock* pipeline should have tagged such objects as QSO but did not, so we expect these misclassifications to be somewhat unusual quasars.

---

[5] When specific outliers are referred to by number (e.g., "outlier 6"), this number denotes their rank based on outlier scores. Identification and coordinates can be found in Table 1.

[6] Objects with AGN activities might not be identified in the BPT diagram if certain lines are inaccessible or if the line profiles are highly non-Gaussian.
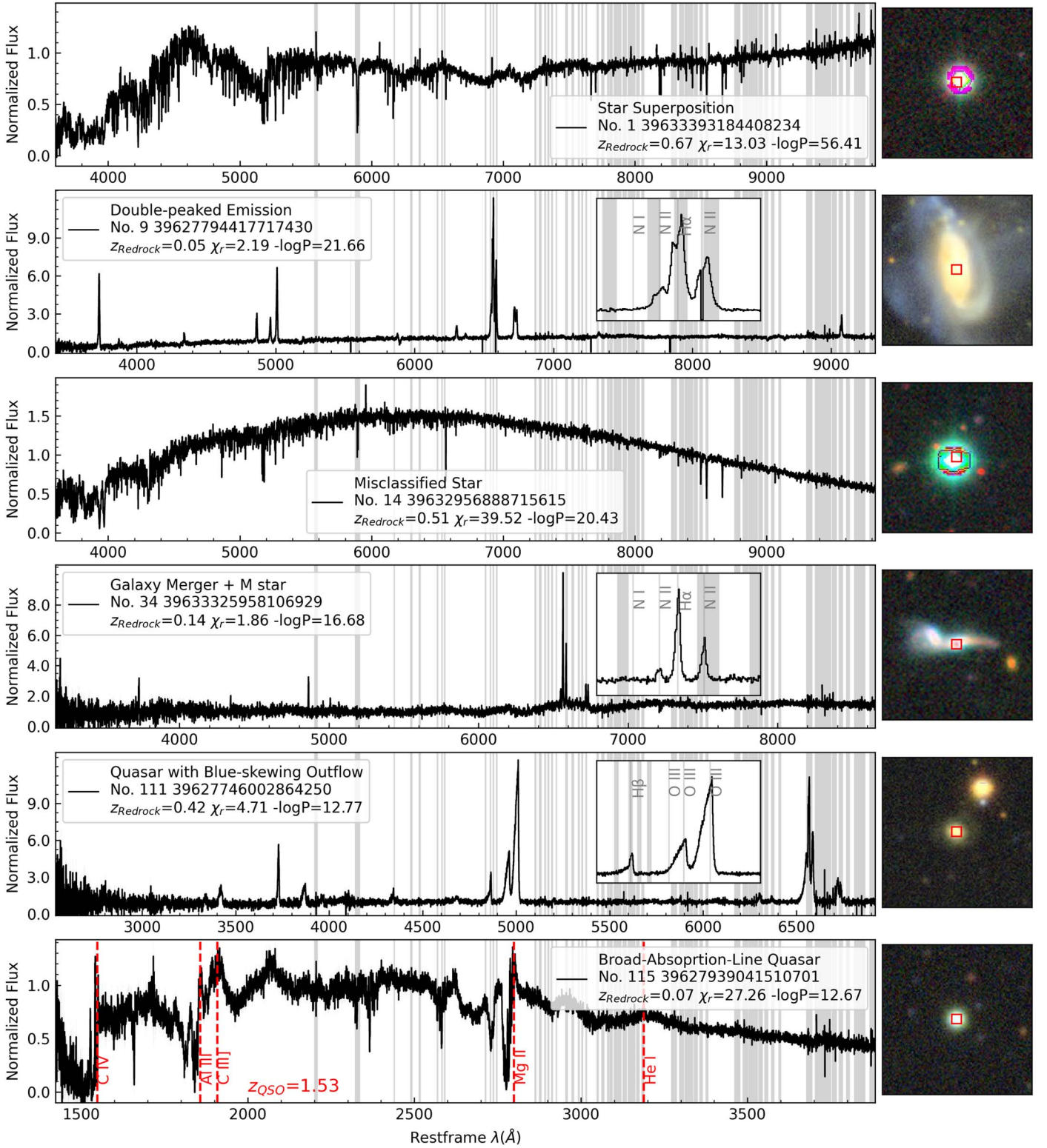
Figure 3. Representative selection of outliers in BGS identified by the galaxy AE and normalizing flow, in decreasing order of the outlier score (details for each object in Section 4). The panels are identical to Figure 2, but for visual clarity, we omitted showing the AE model. The legend in the upper left corner includes the DESI Target ID, *Redrock* redshift, reduced chi-square of the AE model, and the negative log probability of the NF model. The red dashed lines in the bottom panel indicate prominent features of a suspected broad absorption line quasar at $z = 1.53$.

Previously unreported, outlier 111 (fifth row in Figure 3) is characterized by a red/dust-obscured continuum and distinct blue-skewing emission lines, indicating the presence of strong outflows. Its spectral profiles resemble those observed in extremely red quasars (ERQs; Ross et al. 2015; Zakamska et al. 2016). Although this object's broadband color $r - W4 = 12.22$ is not quite as extreme as the previous ERQ criteria ($r - W4 > 14$, where W4 refers to the Vega magnitude in the WISE W4 filter), it is also fainter and toward the low end of the redshift range covered earlier. Its fainter luminosity and lower

redshift align it more closely with the dust-reddened quasars presented by Glikman et al. (2012). In any case, line shapes and photometric properties suggest strongly accelerated gas with high levels of dust obscuration.

Among the two BAL quasars, outlier 29 was recognized as a low-ionization BAL QSO (LoBAL) by Liu et al. (2015). Previously unknown, outlier 115 (last row in Figure 3) has complex and broad absorption features. The *Redrock* redshift estimate of $z = 0.0698$ would render the Hα region highly unusual. Instead, we believe that this source is in fact a BAL (Hall et al. 2002) quasar at $z = 1.53$. This is supported by the presence of deep absorption troughs blueward of Mg II λ2800, C III]λ1909, Al III λ1860, and C IV λ1549. This object bears a resemblance to iron low-ionization BAL quasars (FeLoBALs; Reichard et al. 2003; Choi et al. 2022), a rare subtype of LoBAL quasars that show broad iron absorptions. These FeLoBALs might represent a short-lived transitory phase evolving from young, dust-shielded quasars to more common ones (Farrah et al. 2007), but the origin of the strong absorption lines is still poorly understood.

4.3. Unusual Emission Lines

We identified 42 galaxies that show narrow He II λ4686 emission lines (e.g., outlier 2) or broad emission features at the He II (e.g., outlier 19); both can be interpreted as signatures of Wolf–Rayet stars. Unsurprisingly, the Wolf–Rayet signatures are strongly correlated with extreme starbursts (indicated by the extremely blue continuum) and velocity structures (suggests galactic wind or AGN activity). Previous studies have also reported observations of Wolf–Rayet features in AGNs (Kunth & Contini 1999; Lipari et al. 2003; Brinchmann et al. 2008).

Additionally, the [N I]λ5200 emission line, usually observed in planetary nebulae, was detected in 27 objects, including outlier 9 shown in Figure 3. It also correlates with the aforementioned velocity structures and starburst.

4.4. Extremely Blue/Red Objects

We found that 26 of the top 200 BGS outliers are characterized by an extremely blue continuum, which indicates extreme starbursts.[7] The typical continuum slope for these extremely blue galaxies, obtained by fitting their continuum to a power law $f_\lambda \propto \lambda^\beta$, falls between $-2.5 < \beta < -1$. For context, $\beta = -1$ represents the 0.1% percentile in the BGS galaxy sample. In contrast, only four objects show an extremely reddened continuum. Outlier 83 exhibits such an extreme reddening in its continuum that no emission line bluer than Hα is detected. The corresponding imaging data reveal that the galaxy is in an edge-on orientation with visible dust lanes.

Narrow emission lines (<100 km s^{-1}) are observed in 17 objects (8.5%), and in 12 cases, the imaging data show that they are extragalactic H II regions in nearby galaxies.

4.5. Strong Hδ Absorption

Poststarburst galaxies, commonly known as E + A galaxies, exhibit strong Balmer absorption lines, particularly Hδ absorption. These galaxies have recently experienced a burst of star formation that has subsequently ceased (Goto 2007). Given the transient nature of A-type stars, the E + A phase is

---

[7] This sample excludes nongalactic objects such as stars and quasars.

short-lived in the context of galaxy evolution (Baron et al. 2018).

In our sample, we identified two such galaxies with strong Hδ absorption: outlier 54 (at $z = 0.51$) and outlier 71 (at $z = 0.76$). Notably, both galaxies also present broad [O III] emissions. Specifically, outlier 54 features a "blue wing" adjacent to the [O III] emission, indicative of strong outflow. AGN feedback is proposed as a primary mechanism responsible for terminating star formation in galaxies by expelling the galaxy's remaining gas. The detection of AGN-driven outflows in outlier 54 offers potential evidence of this feedback in action and provides opportunities for further investigation into the feedback process.

4.6. Calibration/Sky-subtraction Issues

Calibration issues, with either a single arm missing or different arms being improperly aligned (e.g., for outlier 4), are detected in 36 objects. A sky-subtraction issue is detected in one object, outlier 90, where a significant portion of flux values are negative.

4.7. Blends

We found a variety of blended objects, similar to the SDSS galaxy outliers we reported in Liang et al. (2023). We present an interesting case, outlier 34, in the fourth row in Figure 3, showing a chance alignment of an M-type star and a distant galaxy merger at $z = 0.13$. We also see star pairs (e.g., outlier 1, first row in Figure 3), a galaxy pair (outlier 125), and a quasar pair (outlier 15).

4.8. Misclassified Star

Among the top 200 outliers in the BGS galaxy sample, the largest group of nongalactic objects consists of 35 stars, including 32 individual stars and 3 star pairs. Outlier 1 (first row of Figure 3) presents the combined spectral features of a K-type star (the Mg b absorption feature) and an M-type star (the red continuum). However, like outlier 14 (third row of Figure 3), many stars we found show no indication of blending and are bright enough to reveal the diffraction spikes and saturate the LS images. We suspect that their brightness led to biases in the imaging measurements, including the estimation of size, which made these objects appear extended and thus targeted in BGS. What surprises us is that *Redrock* classified these sources as galaxies with sufficient confidence (DELTA-CHI2 > 40), sometimes even placing them at cosmological redshifts.

5. Stellar Spectrum Model

We further investigate the stellar contamination in the galaxy sample. A closer inspection of these stellar outliers shows that *Redrock* finds a plausible fit with its galaxy PCA templates, but shows larger residuals for its star templates (see Figure 4). These residuals resemble the prominent metal oxide (TiO, VO) absorption features in M dwarfs, but the residuals flip sign in different sources. As these features cannot arise in emission, we surmise that either the mean PCA spectrum or the eigenvectors *Redrock* uses for its star fits were trained with an overabundance of M dwarfs, so that these metal oxide bands get imprinted on the models of other stars.
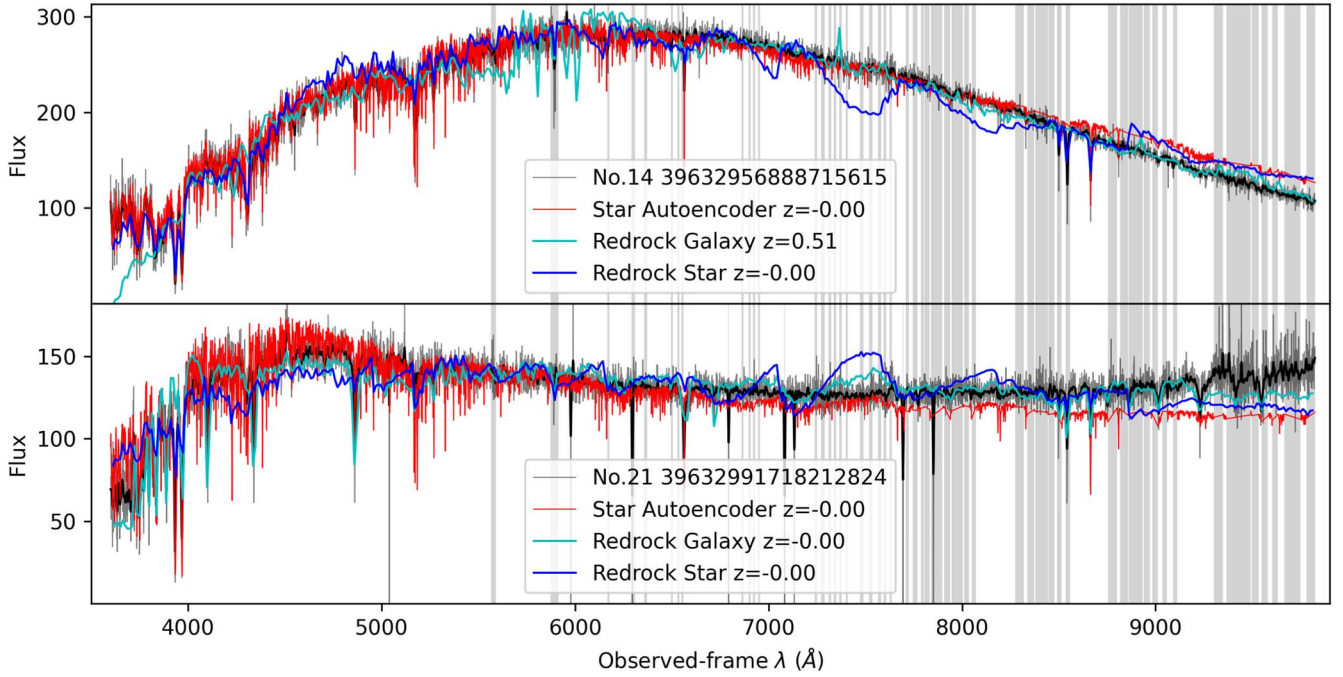
Figure 4. Comparison of observed spectra (black) and model fits (*Redrock* galaxy model (cyan), *Redrock* star model (blue), and our star AE model (red)) for two example stars misclassified as galaxies by *Redrock*. Shaded regions indicate areas masked due to telluric contamination.
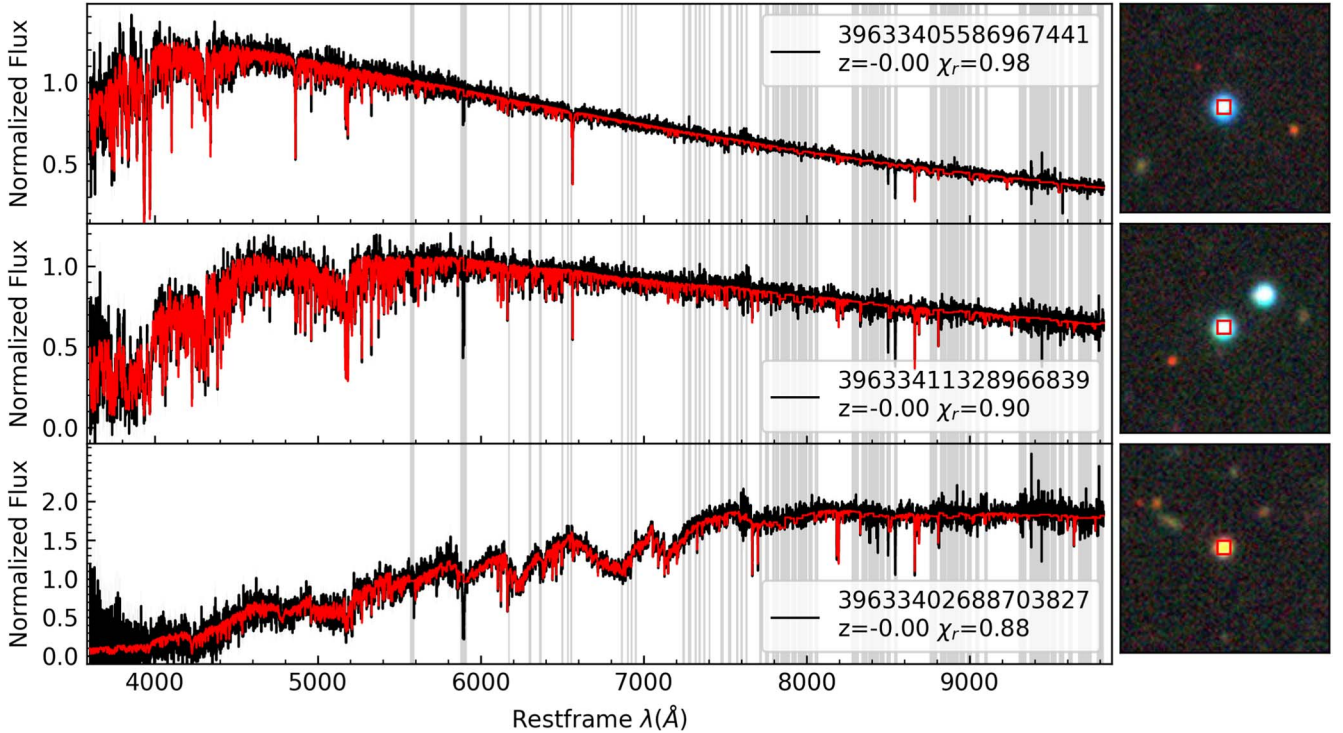

Figure 5. DESI MWS spectra (black) and their reconstructed models (red) from our star AE. Panels as in Figure 2.

To test this hypothesis we make our own star model by following the generative modeling approach of Section 3 and repeat the AE and NF training with stars in the DESI MWS. The typical quality of the StarAE reconstructions of a representative selection of MWS stars can be seen in Figure 5. We also include the StarAE model in Figure 4, demonstrating that it is not affected by the spurious features of the PCA model. We conclude that SPENDER successfully deals with the diversity in stellar types, variations in radial velocity,

and observational imperfections, and produces an accurate model that is not limited to a linear combination of orthogonal templates.

6. Discussion and Conclusions

In this work, we have identified and cataloged outliers from the DESI BGS with a spectrum AE and a normalizing flow. The overall high quality of DESI spectra allows us to present a

rich collection of objects exhibiting unusual physical properties, ranging from irregular or double-peaked emission lines, blended objects, and galaxy mergers, to E + A galaxies with strong outflow, BAL quasars, and reddened quasars. However, our outlier detection scheme has also unveiled issues related to the data collection and processing pipelines. Predominantly, we find BGS outliers to be stars, misclassified by *Redrock* as galaxies.

This finding prompted the development of our own star model, following the same approach as for galaxies, but now applied to stellar spectra from the DESI MWS. We find good modeling quality without the PCA residuals in the current *Redrock* PCA models. We also identified several more outliers that conform neither with our galaxy nor our star model. These are often blended sources, quasars, or spectra with calibration issues.

To facilitate further studies, we release the full catalog of galaxy and star probabilities and reconstruction qualities for all BGS objects at our code repository.[8] The pretrained AE and normalizing flow models are also accessible with instructions at that URL.

As possible extensions of the work presented here, the pretrained StarAE and StarNF models could be employed to identify unusual stars in the MWS sample for follow-up investigations. It is also entirely possible to create a star–galaxy classifier by running a spectrum through both of our pipelines and then comparing the probabilities from each of the NFs to make classification decisions based on the relative likelihoods.

___

[8] https://github.com/pmelchior/spender

Appendix

The Appendix features Table 1, which summarizes the visual classification labels of the top 200 DESI BGS outliers, ranked by their negative log probabilities.

ORCID iDs

Yan Liang ⓘ https://orcid.org/0000-0002-1001-1235
Peter Melchior ⓘ https://orcid.org/0000-0002-8873-5065
ChangHoon Hahn ⓘ https://orcid.org/0000-0003-1197-0902
Jeff Shen ⓘ https://orcid.org/0000-0001-6662-7306
Andy Goulding ⓘ https://orcid.org/0000-0003-4700-663X
Charlotte Ward ⓘ https://orcid.org/0000-0002-4557-6682

References

Astropy Collaboration, Price-Whelan, A. M., Lim, P. L., et al. 2022, ApJ, 935, 167
Astropy Collaboration, Price-Whelan, A. M., Sipőcz, B. M., et al. 2018, AJ, 156, 123
Baron, D., Netzer, H., Prochaska, J. X., et al. 2018, MNRAS, 480, 3993
Bellm, E. C., Kulkarni, S. R., Graham, M. J., et al. 2019, PASP, 131, 018002
Best, P. N., & Heckman, T. M. 2012, MNRAS, 421, 1569
Bolton, A. S., & Schlegel, D. J. 2010, PASP, 122, 248
Brinchmann, J., Kunth, D., & Durret, F. 2008, A&A, 485, 657
Capetti, A., Balmaverde, B., Tadhunter, C., et al. 2022, A&A, 657, A114
Choi, H., Leighly, K. M., Terndrup, D. M., et al. 2022, ApJ, 937, 74
Cooper, A. P., Koposov, S. E., Allende Prieto, C., et al. 2023, ApJ, 947, 37
DESI Collaboration, Adame, A. G., Aguilar, J., et al. 2023a, arXiv:2306.06308
DESI Collaboration, Adame, A. G., Aguilar, J., et al. 2023b, arXiv:2306.06307
DESI Collaboration, Aghamousa, A., Aguilar, J., et al. 2016, arXiv:1611.00036
De Propris, R., Conselice, C. J., Liske, J., et al. 2007, ApJ, 666, 212
Dey, A., Schlegel, D. J., Lang, D., et al. 2019, AJ, 157, 168
Durkan, C., Bekasov, A., Murray, I., & Papamakarios, G. 2020, nflows: normalizing flows in PyTorch, v0.14, Zenodo, doi:10.5281/zenodo.4296287
Farrah, D., Lacy, M., Priddey, R., Borys, C., & Afonso, J. 2007, ApJL, 662, L59
Foreman-Mackey, D. 2016, JOSS, 1, 24
Gaia Collaboration, Brown, A. G. A., Vallenari, A., et al. 2018, A&A, 616, A1
Gaia Collaboration, Brown, A. G. A., Vallenari, A., et al. 2021, A&A, 649, A1
Glikman, E., Urrutia, T., Lacy, M., et al. 2012, ApJ, 757, 51
Goto, T. 2007, MNRAS, 381, 187
Graham, M. J., Kulkarni, S. R., Bellm, E. C., et al. 2019, PASP, 131, 078001
Greenfield, P., Robitaille, T., Tollerud, E., et al. (2013) Astropy: Community Python library for astronomy , Astrophysics Source Code Library, ascl:1304.002
Gugger, S., Lysandre Debut, T. W., Schmid, P., Mueller, Z., & Mangrulkar, S. (2022) Accelerate: Training and Inference at Scale made Simple, Efficient and Adaptable, GitHub, https://github.com/huggingface/accelerate
Guy, J., Bailey, S., Kremin, A., et al. 2023, AJ, 165, 144
Hahn, C., Wilson, M. J., Ruiz-Macias, O., et al. 2023, AJ, 165, 253
Hall, P. B., Anderson, S. F., Strauss, M. A., et al. 2002, ApJS, 141, 267
Harris, C. R., Millman, K. J., van der Walt, S. J., et al. 2020, Natur, 585, 357
Hunter, J. D. 2007, CSE, 9, 90
Kewley, L. J., Dopita, M. A., Sutherland, R., Heisler, C., & Trevena, J. 2001, ApJ, 556, 121
Kim, D. C., Veilleux, S., & Sanders, D. B. 2002, ApJS, 143, 277
Kozieł-Wierzbowska, D., Goyal, A., & Żywucka, N. 2020, ApJS, 247, 53
Kunth, D., & Contini, T. 1999, in IAU Symp. 193, Wolf-Rayet Phenomena in Massive Stars and Starburst Galaxies, ed. K. A. van der Hucht, G. Koenigsberger, & P. R. J. Eenens, 193 (San Francisco, CA: ASP), 725
Lai, T. S.-Y., Smith, J., Baba, S., Spoon, H. W., & Imanishi, M. 2020, ApJ, 905, 55
Lee, N., Sanders, D. B., Casey, C. M., et al. 2015, ApJ, 801, 80
Liang, Y., Melchior, P., Lu, S., Goulding, A., & Ward, C. 2023, AJ, 166, 75
Lipari, S., Terlevich, R., Díaz, R. J., et al. 2003, MNRAS, 340, 289
Liu, W.-J., Zhou, H., Ji, T., et al. 2015, ApJS, 217, 11
Melchior, P., Liang, Y., Hahn, C., & Goulding, A. 2023, AJ, 166, 74
Nordin, J., Brinnel, V., Giomi, M., et al. 2020, Transient Name Server Discovery Report 2020-624

Papamakarios, G., Pavlakou, T., & Murray, I. 2017, in 31st Conf. on Neural Information Processing Systems (NIPS 2017) (Red Hook, NY: Curran Associates, Inc.) https://proceedings.neurips.cc/paper_files/paper/2017/file/6c1da886822c67822bcf3679d04369fa-Paper.pdf

Paszke, A., Gross, S., Massa, F., et al. 2019, in 33rd Conf. on Neural Information Processing Systems (NeurIPS 2019) (Red Hook, NY: Curran Associates, Inc.) https://proceedings.neurips.cc/paper_files/paper/2019/file/bdbca288fee7f92f2bfa9f7012727740-Paper.pdf

Reichard, T. A., Richards, G. T., Hall, P. B., et al. 2003, AJ, 126, 2594

Renzini, A., & Peng, Y.-j 2015, ApJL, 801, L29

Ross, N. P., Hamann, F., Zakamska, N. L., et al. 2015, MNRAS, 453, 3932

Sainburg, T., McInnes, L., & Gentner, T. Q. 2021, Neural Comput., 33, 2881

Shen, Y., Liu, X., Greene, J. E., & Strauss, M. A. 2011, ApJ, 735, 48

Tabak, E. G., & Turner, C. V. 2013, CPAM, 66, 145

Tabak, E. G., & Vanden-Eijnden, E. 2010, Commun. Math. Sci., 8, 217

York, D. G., Adelman, J., Anderson, J. E., Jr, et al. 2000, AJ, 120, 1579

Zakamska, N. L., Hamann, F., Pâris, I., et al. 2016, MNRAS, 459, 3144